Platinum and Platinum Group Metal-Free Catalysts for Anion Exchange Membrane Fuel Cells

Van Men Truong [1], Julian Richard Tolchard [2], Jørgen Svendby [3], Maidhily Manikandan [3], Hamish A. Miller [4], Svein Sunde [3,*], Hsiharng Yang [1,*], Dario R. Dekel [5,*] and Alejandro Oyarce Barnett [2,6,*]

[1] Graduate Institute of Precision Engineering, National Chung Hsing University, Taichung 40227, Taiwan; mentruong0101@gmail.com

[2] Sustainable Energy Department, SINTEF Industri, Postboks 4760 Torgarden, 7465 Trondheim, Norway; JulianRichard.Tolchard@sintef.no

[3] Department of Materials Science and Engineering, Norwegian University of Science and Technology, NO-7491 Trondheim, Norway; jorgen.svendby@ntnu.no (J.S.); maidhily.manikandan@ntnu.no (M.M.)

[4] Istituto di Chimica dei Composti Organometallici (CNR-ICCOM), via Madonna del Piano 10, 50019 Sesto Fiorentino, Firenze, Italy; hamish.miller@iccom.cnr.it

[5] The Wolfson Department of Chemical Engineering and the Nancy & Stephan Grand Technion Energy Program (GTEP), Technion, Israel Institute of Technology, Haifa 3200003, Israel

[6] Department of Energy and Process Engineering, Norwegian University of Science and Technology, NO-7491 Trondheim, Norway

* Correspondence: svein.sunde@ntnu.no (S.S.); hsiharng@dragon.nchu.edu.tw (H.Y.); dario@technion.ac.il (D.R.D.); AlejandroOyarce.Barnett@sintef.no (A.O.B.)

check for updates

Abstract: The development of active hydrogen oxidation reaction (HOR) and oxygen reduction reaction (ORR) catalysts for use in anion exchange membrane fuel cells (AEMFCs), which are free from platinum group metals (PGMs), is expected to bring this technology one step closer to commercial applications. This paper reports our recent progress developing HOR Pt-free and PGM-free catalysts (Pd/CeO$_2$ and NiCo/C, respectively), and ORR PGM-free Co$_3$O$_4$ for AEMFCs. The catalysts were prepared by different synthesis techniques and characterized by both physical-chemical and electrochemical methods. A hydrothermally synthesized Co$_3$O$_4$ + C composite ORR catalyst used in combination with Pt/C as HOR catalyst shows good H$_2$/O$_2$ AEMFC performance (peak power density of ~388 mW cm^{-2}), while the same catalyst coupled with our flame spray pyrolysis synthesised Pd/CeO$_2$ anode catalysts reaches peak power densities of ~309 mW cm^{-2}. Changing the anode to nanostructured NiCo/C catalyst, the performance is significantly reduced. This study confirms previous conclusions, that is indeed possible to develop high performing AEMFCs free from Pt; however, the challenge to achieve completely PGM-free AEMFCs still remains.

Keywords: non-Pt electrocatalyst; non-PGM electrocatalyst; hydrogen oxidation reaction; oxygen reduction reaction; alkaline fuel cell

1. Introduction

Fuel cells are excellent energy convertors due to their advantages of high efficiency and high energy density, and have the potential to provide continuous zero-emission power. Among the different alternatives, anion exchange membrane fuel cells (AEMFCs) have been identified as a promising fuel cell technology, due to their potential advantages over the mature proton exchange membrane fuel cells [1,2], which include the possibility of using non-noble metals as electrode catalysts due to the faster oxygen reduction reaction (ORR) kinetics in alkaline media [3,4]. A wide variety of catalysts

may be used as ORR catalysts in AEMFC cathodes [5,6]. Among the non-precious metal catalysts for the cathode, Ag (or Ag/C) is the most widely used catalyst for AEMFCs [7,8]. However, Co-based catalysts in the form of Co_3O_4, have also been recognized as potential ORR catalytic materials due to their low cost, good electrical conductivity, and stability in alkaline media [9–11]. For instance, Xu et al. [12] prepared carbon-supported Co_3O_4 electrocatalysts with nano-rod and spherical structures via a solvent-mediated morphological control route, showing only slightly lower ORR catalytic activity than that measured with the noble Pd catalyst in the high potential region. Wang et al. [13] synthesized Co_3O_4 clad with graphene oxide (Co_3O_4@GO) by an ultrasonic method, which showed potentially good characteristics as a low-cost catalyst for ORR in AEMFCs. Liang et al. [14] reported that the catalytic behavior of Co_3O_4 grown on reduced graphene oxide (RGO) exhibits good activity towards ORR in alkaline electrolyte, close to that of Pt/C. These ex-operando results suggest that Co_3O_4 is a promising platinum group metal (PGM)-free electrocatalyst for ORR in AEMFCs. However, limited work has been reported on the performance of Co_3O_4-based ORR catalysts as real AEMFC cathodes [9,15,16].

Although the alkaline environment in AEMFCs potentially allows the use of Pt-free catalysts for ORR, the hydrogen oxidation reaction (HOR) kinetics in alkaline media are considerably more sluggish than for acidic media [10]. The HOR has several challenges in the alkaline medium [11]. A comprehensive review summarizing the development efforts over the past decades on HOR catalysts in alkaline medium was recently reported [17]. In this regard, Pd-based electrocatalysts have emerged as one of the few options for Pt-free AEMFCs [18,19]. A new class of Pd-based materials that exploit mixed carbon and cerium oxide supports has been reported to have excellent performance as anode catalysts in AEMFCs, with reported power densities of 0.5–1 W cm^{-2} [20,21]. In particular, the addition of CeO_2 to Vulcan XC-72 carbon with a 50:50 weight ratio to support Pd nanoparticles was reported to yield a 5-fold improvement in anode performance when compared to Pd supported on carbon catalyst (without ceria) under the same fuel cell operating conditions. Miller et al. [18] posit that the presence of intimate contact between CeO_2 and Pd enhances the OH^- transfer from the anion-conducting regions in the anode electrode to the metal surface where the HOR takes place.

For PGM-free fuel cells, Ni-based electrocatalysts seem like a reasonable catalyst choice [21,22]. Various studies on Ni-based materials (Raney Ni, Ni-Cr, Ni-Ti, etc.) have found them to be suitable as anode catalysts when the electrolyte is liquid KOH. However, only limited work has been devoted to the development of Ni-based HOR catalysts for AEMFCs, where only a solid polymer electrolyte is present. The first fully PGM-free AEMFC test was demonstrated by Lu et al. [23] using a chromium doped Ni anode and Ag cathode. A maximum power density of 50 mW cm^{-2} at 60 °C was achieved without any degradation over 100 h. Another study by Hu et al. [24] showed a Ni-W anode and Co-based cathode for H_2/O_2 and H_2/air AEMFCs, reaching peak power densities of around 40 mWcm^{-2} and 27 mWcm^{-2} respectively, demonstrating, for the first time, the potential of using PGM-free catalysts for AEMFCs. More recently, excellent performance has been demonstrated using NiMo/C [25] and NiCu/C [26] as anode catalyst, using the PGM Pd/C as cathode catalyst, showing AEMFC peak power densities of 120 mW cm^{-2} and 150 mW cm^{-2}, respectively.

The present study deals with the development of the next generation of materials focusing on affordable and abundant catalyst materials for AEMFCs. In particular, three catalysts for the anodic HOR are compared, including: (i) The state-of-the-art 10 wt % Pd/C-CeO_2 catalyst [18], (ii) a compositionally equivalent 10 wt % Pd/CeO_2 + C catalyst in which a Pd-CeO_2 nanocomposite is produced through a one-pot flame spray pyrolysis (FSP) synthesis before mixing with Vulcan XC-72, here denoted as "FSP Pd/CeO_2 + C", and (iii) a nanostructured 50 wt % Ni_3Co alloy supported on Vulcan XC-72 (NiCo/C). The AEMFC cathode catalyst consists of Co_3O_4 prepared by hydrothermal synthesis and later mixed with Vulcan XC-72 ("Co_3O_4 + C"). The synthesized Pt-free catalysts were comprehensively characterized for their physicochemical properties using X-ray diffraction (XRD), transmission electron microscopy (TEM), and X-ray photoelectron spectroscopy (XPS) techniques. The paper focuses on the initial catalytic performance and kinetics of these catalysts towards HOR or ORR through conventional wet electrochemical methods, as well as their performance when

integrated into AEMFC single cells using commercially available gas diffusion layers (GDLs), anion exchange membranes (AEMs) and ionomer. Here, the catalysts are evaluated for their beginning-of-life performance in H_2/O_2 AEMFCs single cells.

2. Results and Discussion

2.1. Physical Characterization

2.1.1. Physical Characterization of the Co_3O_4 ORR Catalyst

Figure 1c shows the fitted XRD for the cobalt oxide product phase after heat treatment at 250 °C in air, with fitted diffraction data for the cobalt carbonate precursor presented in the Supplementary Information (Figure S1). It is seen that the cobalt carbonate precursor forms as agglomerated platelets of an individual size of less than 10 μm (Figure 1a). Ball milling breaks up these agglomerates effectively, and it is confirmed that following heat-treatment, a product phase is obtained which comprises FCC nanoparticles in the order of 10–20 nm in size, arranged in highly anisotropic "platelets" which are up to micron-sized in two dimensions, but are only 1–3 particles in thickness (Figure 1b,d). The powder XRD pattern (Figure 1c) confirms that the sample is a single spinel structured Co_3O_4, with a fitted unit cell parameter of a = 8.0846(8) Å [27]. A volume-weighted crystallite size of 13.5(3) nm was calculated via whole powder pattern fitting of the peak profiles.
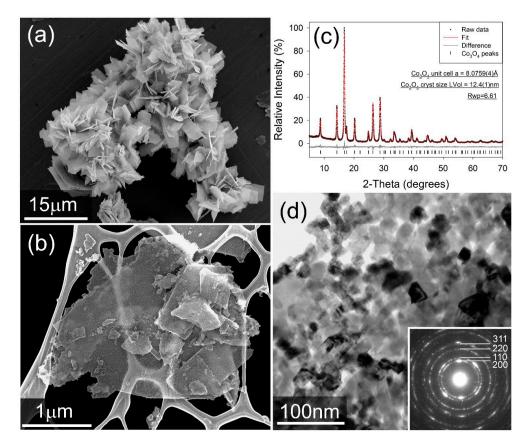

Figure 1. (**a**) Secondary electron image of as-made $Co_2(CO_3)OH_2$. (**b**) secondary electron image of the milled Co_3O_4 catalyst. We note that the sample was mounted on a Lacey Carbon TEM grid for imaging. (**c**) Fitted X-ray diffractogram for the Co_3O_4 catalyst. Data were collected in capillary transmission mode using a Mo-K$_\alpha$ source and modelled using a Rietveld-type approach. (**d**) bright-field TEM image of Co_3O_4 catalyst particles. Inset: Selected-area electron diffraction pattern, showing rings consistent with an FCC lattice.

2.1.2. Physical Characterization of the HOR Catalysts

Figure 2b–g display the annular dark field STEM images and associate chemical maps for the 10 wt % Pd/C-CeO$_2$ catalyst. The catalyst is a mixed composite of crystalline Pd particles of size <10 nm, CeO$_2$ agglomerates in the 10–40 nm size range, and carbon particles of around 50–70 nm. The CeO$_2$ particles and Pd particles appear to be quite well distributed on the carbon support but are not strongly associated with each other.
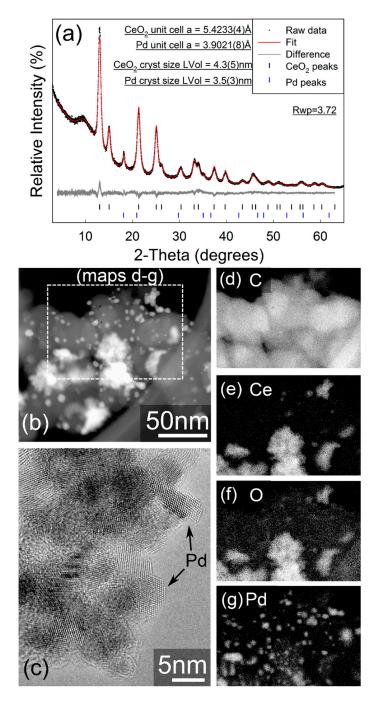

Figure 2. (**a**) Fitted X-ray powder diffractogram for Pd/C-CeO$_2$. Data were collected in capillary transmission mode using a Mo-K$_\alpha$ source and modelled using a Rietveld-type approach. The "amorphous bump" at approx. 9° 2θ is due to the Kapton capillary material. (**b**) Annular dark-field STEM image, (**c**) high-resolution TEM image showing crystalline Pd particles, (**d**–**g**) elemental EDX images acquired within the area indicated in (**b**). Gamma adjustments were applied in (**b,d**–**g**).

In contrast, the STEM imaging and EELS element mapping for the as-synthesized FSP Pd/CeO_2 sample (Figure 3b–e) show an extremely even distribution of Pd and CeO_2, which is a consequence of the single step FSP synthesis. The FSP sample also demonstrates regions of Pd enrichment which show no apparent crystallinity and are sufficiently small (~1 nm) that it is unclear whether these can even be considered as formal particles, and the Pd in a separate phase to the CeO_2. The 10 wt % $Pd/C-CeO_2$ catalyst has previously been characterized by XRD, XAS and other techniques [18–21]. However, the XRD data for both the 10 wt % $Pd/C-CeO_2$ and as-synthesizes FSP Pd/CeO_2 may be compared in Figures 2a and 3a, respectively. For both samples nanocrystalline CeO_2 is observed, with calculated crystallite sizes of 4.35(5) nm and 3.08(3) nm calculated for the 10 wt % $Pd/C-CeO_2$ and FSP Pd/CeO_2 samples, respectively. Similar unit cell parameters of a = 5.4230(4) Å and a = 5.4263(4) Å are obtained for the CeO_2 phase in the two respective samples. For the 10 wt % $Pd/C-CeO_2$ sample, relatively sharp diffraction lines due to crystalline Pd are also observed, which suggests that a portion of the Pd in this sample has a much larger particle/crystallite size than that observed by electron microscopy. No evidence of a crystalline Pd-containing phase is observed in the diffraction data for the FSP Pd/CeO_2 sample.
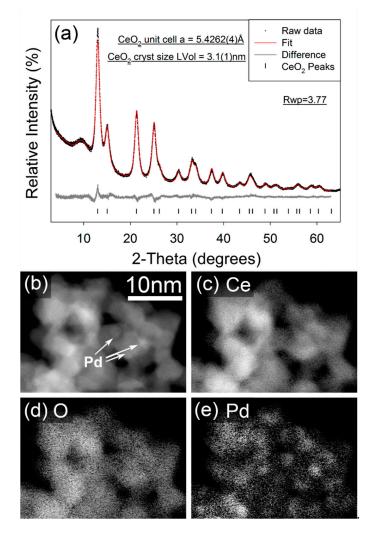

Figure 3. (**a**) Fitted X-ray powder diffractograms for FSP synthesized FSP Pd/CeO_2. Data were collected in capillary transmission mode using a Mo-K$_\alpha$ source and modelled using a Rietveld-type approach. The "amorphous bump" at ~9° 2-Theta is due to the Kapton capillary material, (**b**) STEM image, and (**c**–**e**) elemental EELS maps from FSP Pd/CeO_2.

XPS data are presented in Figure 4a–d, with a summary of the Pd $3d_{5/2}$ binding energies presented in Table 1. Both samples show Ce(3d) spectra with binding energies characteristic of both Ce(IV) and Ce(III) species. Based on relative areas a ratio of approximately 70:30 is determined. However, the fitting and quantification of CeO_2, especially CeO_2 nanoparticles, are known to be challenging and unreliable, due to the heavy peak overlap in the spectra and surface stabilization of Ce(III). This causes a general over-estimation of the Ce(III) content in CeO_2 nanomaterials, and can easily lead to misinterpretation of results [28,29]. Consequently, only a limited conclusion is drawn: That there are no significant differences between the Ce spectra of the 10 wt % Pd/C-CeO_2 and FSP Pd/CeO_2 samples. In contrast, the Pd XPS spectra show marked differences between the samples. The 10 wt % Pd/C-CeO_2 Palladium spectrum in Figure 4a can be deconvoluted in terms of three Pd $3d_{5/2}$/$3d_{3/2}$ doublets, while the FSP Pd/CeO_2 sample in Figure 4b is predominantly a single doublet, with a small fraction of a second species present.
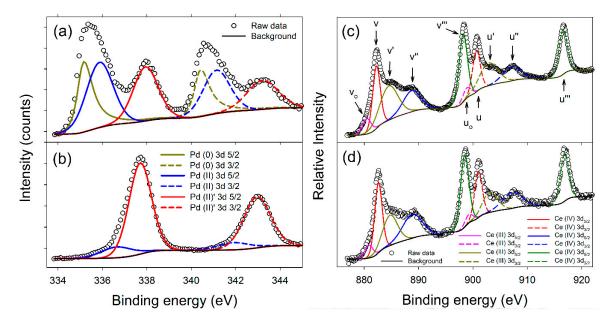

Figure 4. XPS data for Pd for (**a**) Pd/C-CeO_2, and (**b**) FSP Pd/CeO_2. Lines marked Pd(0), Pd(II) and Pd(II) are assigned respectively to metallic Pd, sub-stoichiometric PdO and super-stoichiometric PdO. XPS data for Ce for (**c**) Pd/C-CeO_2, and (**d**) FSP Pd/CeO_2. To aid comparison with previous work, the commonly used nomenclature of Burroughs et al. [30] was adopted in (**c**).

Table 1. Normalized Pd $3d_{5/2}$ binding energies for the Pd/C-CeO_2 and FSP 18%Pd/CeO_2 samples.

Pd	10 wt % Pd/C-CeO_2	FSP 18%Pd/CeO_2	Ref [31,32]
Pd(0)	335.2	N/A	335.1–335.4
Pd(II)	335.9	336.7	336.7–336.8
Pd(II)	337.9	337.7	see main text

Bulk Pd$3d_{5/2}$ lines are reported in the range E_b(Pd $3d_{5/2}$) = 335.1 to 335.4 eV, and bulk PdO values in the range E_b(Pd $3d_{5/2}$) = 336.7 to 336.8 eV [31,32]. Following these, the lowest energy line observed in the 10 wt % Pd/C-CeO_2 spectrum is assigned to metallic Pd, and the line at E_b = 335.9 eV to a sub-stoichiometric PdO_{1-x} species, due to the shift in binding energy (BE) relative to PdO. The FSP-synthesized FSP Pd/CeO_2 shows no evidence of metallic Pd, and only a weak signal which can similarly be attributed to a PdO-type Pd(II) signal (Figure 4b). This peak is broad though, and likely also describes some sub-stoichiometric PdO_{1-x}. Both the 10 wt % Pd/C-CeO_2 and FSP Pd/CeO_2 samples exhibit strong lines at a higher BE that can be attributed to a PdO type species, and at a similar energy to that for Pd(IV) [33,34]. This line is labelled Pd(II) so as to avoid confusion, as the composition PdO_2

is not stable under the conditions of the sample preparation, and the presence of a formal Pd^{4+} bulk oxide cannot be concluded. Nevertheless, the high BE does indicate a high level of charge transfer from the Pd. Several authors have reported Pd $3d_{5/2}$ lines with similar binding energies for supported Pd catalysts [35,36]. Most ascribe the shift to a higher BE to an interaction between the catalyst and CeO_2 support, though it is documented that for metallic systems a reduction in particle size at the extreme nano-scale can cause a shift to higher binding energies [37,38].

Figure 5a shows the fitted X-ray diffraction pattern for the PGM-free NiCo/C catalyst after annealing at 500 °C. The diffraction pattern for the sample, prior to annealing, is given in the Supplementary Information (Figure S2). The observed pattern after annealing can be fitted to a FCC unit cell with unit cell parameter a = 3.5306(5) Å, which corresponds well to a composition of approximately $Ni_{0.6}Co_{0.4}$ [39]. A broad region of unfitted intensity is also evident around the (100) reflection. The position of this correlates with that expected for the hexagonal crystal structure for Co or a Cobalt-rich Co-Ni, though the presence of no well-defined maxima suggests a high level of faulting or structural disorder in the hexagonal fraction. The cubic to hexagonal transformation, and concomitant formation of high stacking fault density is well known in the pure cobalt system [40]. It has also been reported that there is a strong correlation between particle size and the favored crystalline polymorph of Co, with the cubic phase being stable below a particle diameter of ~20 nm and a mixture of hexagonal and cubic phases being favored above that [41]. The NiCo catalyst in this study are spherical in morphology and are dispersed onto the carbon surface. The catalyst particles tend to agglomerate after annealing, resulting in an increased nanoparticle size from 7–10 nm range (pristine) to 15–20 nm (after annealing). The resulting particle size and size distribution of the catalyst after annealing may be seen in the bright and dark field images of NiCo/C (Figure S3). Figure 5b,c further show the HAAD-STEM image, as well as the corresponding STEM-EDX elemental line scan and mapping. The characterization data confirm that the NiCo nanoparticles consist of an alloy of Ni and Co, with the EDS line scan showing relatively homogeneous composition across the particle, with a slight Ni-enrichment suggested at the core. The measured particle composition is slightly more Ni-rich than that suggested by the unit cell parameter calculated from the XRD data. Also observed in the EDS data (but not shown), was the presence of a small amount of phosphorous on the surface of the alloys. Similar results of unpremeditated formation of P dopants and/or impurities were reported elsewhere [42].

In order to obtain further information about the surface of the alloy, XPS analysis was carried out. The deconvoluted spectra for both the Ni $2p_{3/2}$ and Co $2p_{3/2}$ are shown in the Supplementary Information Figure S4. The spectra consist of both Ni and Co at various oxidation states. Ni peaks at binding energies of 852.81 ± 0.1 eV and 854.72 ± 0.1 eV are respectively attributed to metallic Ni^0 and Ni^{2+} in the form of NiO [43]. The line centered at 856.05 ± 0.1 eV could either be due to Ni_2O_3 or $Ni(OH)_2$ and a shake-up satellite peak at 861.26 ± 0.1 eV are within the reported literature values [44,45]. A small peak at BE 858.66 ± 0.1 eV can be denoted as the peak due to the alloying of Ni with secondary metal [46]. Five peaks are fitted for Co $2p_{3/2}$, where the main BE at 781.39 ± 0.1 eV and its ratio with corresponding satellite peak centered at 786.68 ± 0.1 eV indicate a Co^{3+} oxidation state and/or hydroxide form of Co [47,48]. The peak corresponding to metallic Co is observed at 777.91 ± 0.1 eV, and the two other peaks fitted at 780.66 ± 0.1 eV and 784.11 ± 0.1 eV may be attributed to Co^{2+} oxide and the Co-Ni interaction [49]. The presence of oxides is unavoidable as the catalysts are stored and handled under ambient conditions. A surface pre-treatment is performed prior to the HOR measurements in half-cell, which is intended to reduce the metallic surface. The reducing environment under H_2 in electrolyte should also be a favorable condition to control the surface passivation during the measurements.
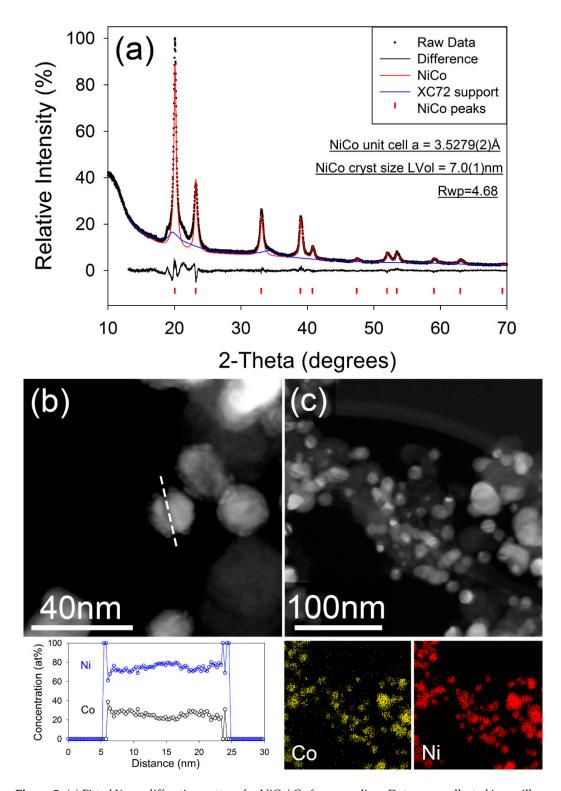
Figure 5. (**a**) Fitted X-ray diffraction pattern for NiCo\C after annealing. Data were collected in capillary transmission mode using a Mo-K$_\alpha$ source and modelled using a Rietveld-type approach. (**b**) Dark field image of annealed NiCo/C nanoparticles, with composition measured along the dashed line. (**c**) Dark field STEM image of annealed NiCo/C nanoparticles with corresponding X-ray element maps of Co (yellow), and Ni (red).

2.2. Electrochemical Characterization

2.2.1. RRDE Characterization of Co_3O_4

Figure 6a shows the cyclic voltammograms (CVs) and the ORR activity of the Co_3O_4 + C composites compared to Pt/C catalysts in Argon saturated 0.1 M KOH electrolyte. The shape and peak positions of the Pt/C CV is consistent with the literature on Pt/C catalysts in 0.1 M KOH. The two CVs of the Co_3O_4 catalyst, using two different catalyst loadings, differ considerably from the voltammogram of Pt/C catalyst. Co_3O_4 show a typical double layer capacitive behavior and the absence of redox reactions. The absence of hydrogen absorption/desorption peaks, as well as Pt oxidation peaks are clear indications that there is no, or a negligible amount of dissolved Pt in the system that may have originated from Pt counter electrode dissolution and redeposition on the working electrode. It has recently been shown, that Pt dissolution of the counter electrode is considerably minimized in an alkaline environment [50]. It is, however, strongly recommended that for long-term measurements, recently recommended best practices are implemented [51].

The current density of the 460 µg Co_3O_4 electrode is approximately double the magnitude of the current density of the 230 µg Co_3O_4 electrode, which is consistent with expectations from doubling the electrode mass. Figure 6c shows the ORR activity in O_2-saturated 0.1 M KOH solution with an anodic scan sweep taken at a rotating speed of 1600 rpm and at 20 mV s^{-1}. The Pt/C showed the highest ORR onset potential of 0.854 V vs reversible hydrogen electrode (RHE), defined as the potential at 0.1 mA cm^{-2}. Although this value is slightly lower compared to the optimized values of Campos-Roldan et al. [52], the activity is well within the values previously reported in the literature [52]. The PGM-free Co_3O_4 catalyst shows relatively good catalytic activity towards the ORR, with onset potentials of 0.684 V for both the 460 µg Co_3O_4 and 230 µg Co_3O_4 loadings. In these experiments, the addition of more catalyst does not seem to affect the catalytic activity at high potentials. But, the limiting current density increased significantly with the addition of more Co_3O_4 catalyst. Higher electrode loadings also influence the ring current, resulting in lower peroxide yields (Figure 6b). Calculated from the ring current of the Pt/C electrode, the formation of HO_2^- by the four-electron reduction of O_2 is obvious (electron transfer number of 3.99–3.98 going from high to low potentials). For the Co_3O_4 catalyst, however, the electron transfer number was lower at ~3.98–3.92 for the 460 µg Co_3O_4 electrode and ~3.94–3.87 for the 230 µg Co_3O_4. The mass activity, on the other hand, is considerably lower for Co_3O_4 catalysts as compared to Pt/C. At 0.85 V the mass activity for the Pt/C is approximately 11 A g^{-1}, whilst both Co_3O_4 electrodes, independent of the electrode loading, showed mass-activities three orders of magnitude lower than the Pt/C catalysts, in the region of 0.06 A g^{-1}.

2.2.2. RDE Characterization of HOR Catalysts

The catalytic activities of the Pt/C, 10 wt % Pd/C-CeO$_2$, FSP Pd/CeO$_2$ + C and NiCo/C catalysts towards HOR in 0.1M KOH are compared in Figure 7, Figures S5 and S6. Figure 7 shows the currents during a voltammetric scan at 5 mV s^{-1} in hydrogen-saturated solutions, with the catalysts deposited on a rotating disc electrode (RDE) rotating at 1600 rpm. The catalyst loading was 0.5 mg metal for the NiCo/C catalyst and 0.05 mg for the PGM catalysts.

Currents normalized both with respect to the geometric surface area of the electrode (Figure 7a) and the mass of the catalyst deposited on the RDE (Figure 7b) are shown. The current normalized with respect to the geometric surface area is in the same order of magnitude for all catalysts. The Pd/CeO$_2$ catalysts and the Pt/C catalysts display a similar performance overall, including a well-defined limiting current beyond 0.2 V. The current from the 10 wt % Pd/C-CeO$_2$ catalyst, however, overshoots and displays a pronounced peak at 0.15 V, beyond which it decreases to the same limiting current as the FSP Pd/CeO$_2$ + C and Pt/C catalysts. Owing to the much larger mass of the NiCo/C catalyst, the mass activity of this catalyst is much smaller than those of the other catalysts, as shown in Figure 7b.
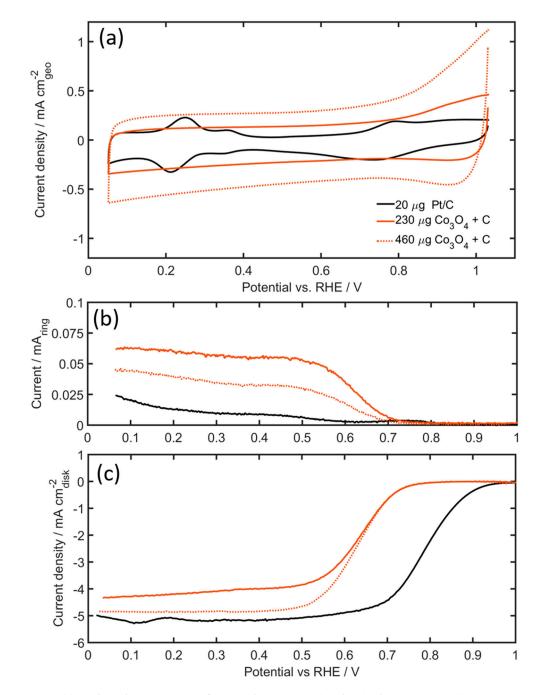
Figure 6. (**a**) Cyclic voltammograms of Pt/C and Co_3O_4 + C (catalyst/carbon ratio = 1.25) in Ar-saturated electrolyte, (**b**) Rotating ring disk electrode (RRDE) ring current during ORR, and (**c**) disk current during ORR of Pt/C and Co_3O_4 + C (catalyst/carbon ratio = 1.25) in O_2-saturated electrolyte. Disk current are both iR corrected (using electrochemical impedance spectroscopy (EIS) and background corrected (using CV currents from Figure 6a). All measurements performed in 0.1 M KOH, rotating speed: 1600 rpm, scan rate: 20 mVs^{-1}, using catalyst loadings of 20 µg Pt, 230, and 460 µg of Co_3O_4.
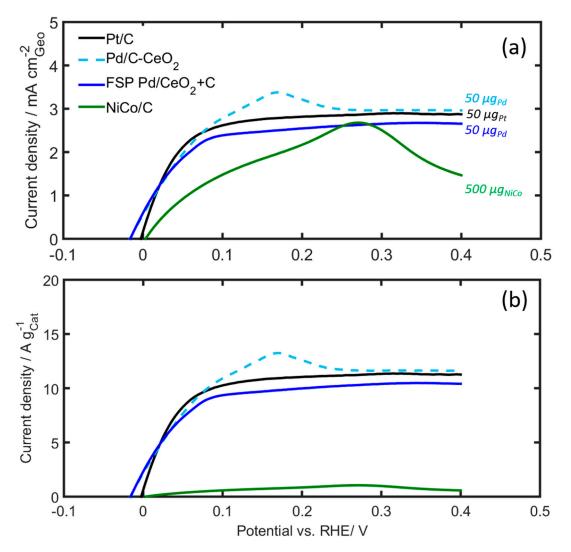
Figure 7. RDE voltammograms of Pd/C-CeO$_2$, Pd/CeO$_2$ + C and NiCo/C compared to Pt/C in H$_2$-saturated 0.1 M KOH. (**a**) Geometric current density, and (**b**) mass specific current density. Scan rate: 5 mV/s, rotating speed: 1600 rpm. The catalyst loading was 500 μg based on NiCo, and 50 μg for the PGM catalysts.

It is worth noticing that beyond 0.3 V there is a sharp decline in the observed NiCo/C current (see Figure 7a), presumed to be due to reactions forming NiOH and Ni(OH)$_2$ at the catalyst surface, which passivate the surface from further hydrogen oxidation [25,53]. Kabir, S. et al. [25] also observed a HOR current decay at potentials above 0.12 V for NiMo, without reaching the diffusion limiting value as observed for Pt electrodes. This was attributed to the blocking of the Ni surface by α-Ni(OH)$_2$. The authors also performed a micro kinetic model able to reproduce and explain these results. Recently, Davydova et al. [53] studied the stability of Ni$_3$M/C HOR catalysts (M = Co, Fe, Cu, Mo) in alkaline medium, using in situ and ex situ techniques, as well as online ICP-MS. The results showed that no Ni or Co dissolution was observed from Ni/C, Ni$_3$Co/C, still neither of the catalysts was found to be electrochemically active toward the HOR after prolonged potential cycling to a potential higher than 0.3 V vs RHE. The authors attribute these phenomena to a "dissolution−precipitation" mechanism that results in the formation of Ni(OH)$_2$ layered octahedral sheets representing the most thermodynamically favored phase/crystal.

Figure S5 further shows the CVs of the NiCo/C in Ar and H$_2$-saturated solutions in more detail. The voltammograms in the Ar-sparged solutions demonstrate the typical features for bulk Ni [54,55], with forward wave peaking at 0.2 V, representing the formation of α-Ni(OH)$_2$. On the reverse scan

the current is small, negative and constant down to approximately 0.15 V, at which point the onset of the reduction of α-Ni(OH)$_2$ appears and results in a cathodic peak at 0.05 V. In the H$_2$-saturated electrolyte, the current increased significantly in the forward scan, which we assign to the oxidation of H$_2$. Here, the current increases until the potential reaches 0.21 V. On the reverse scan in the hydrogen-saturated solution, the current is close to zero in the potential range 0.3 V through 0.15 V, which is a good indication that the working electrode is not contaminated by the possible Pt dissolution from the counter electrode: Any redeposited Pt would have resulted in clear and high H$_2$ oxidation currents. As the potential reaches 0.15 V, an anodic wave appears in the H$_2$-saturated electrolyte, also apparent on the return sweep, peaking at approximately 0.05 V. The onset potential for the anodic wave on the return sweep is approximately the same as that for the reduction of α-Ni(OH)$_2$ in the voltammogram in the argon-saturated solution. We therefore associate the reverse-scan oxidation process with hydrogen oxidation at catalyst surface freed from α-Ni(OH)$_2$ as the potential is decreasing. The reverse-scan hydrogen oxidation wave coincides with the current in the forward sweep as the potential approaches zero.

2.3. AEMFC Results

Figure 8 shows the fuel cell polarization curves and power density curves obtained for the AEMFCs with the Pt-free and PGM-free catalysts. The cells are operated at 70 °C under H$_2$ and O$_2$ gases with controlled dew points of 68 °C and 73 °C for the anode and cathode, respectively. The PGM-free Co$_3$O$_4$ + C shows good performance as a cathode catalyst, when using Pt/C on the anode, and when compared to the PGM-Pt cathode only a 20 mV difference at open circuit voltage (OCV) is observed, and approximately a 35 mV difference at 50 mA cm^{-2}, see also Figure S7. It is noticed that the voltage difference is significantly smaller compared to the RDE measurements in liquid KOH, which shows a 170 mV difference at 10 mA cm^{-2} (see Figure 6c). Mamlouk et al. [15] reported similar results for their Co-based catalysts, e.g., a 50 mV difference at 50 mA cm^{-2} between Co-based and Pt ORR catalysts in AEMFC, while observing a 120 mV difference in RDE. Figure 8 further shows that at higher current densities, the cell voltage difference at 0.5 A cm^{-2} between the two cells is only 110 mV, i.e., 0.7 V and 0.59 V, for the Pt/C and Co$_3$O$_4$ + C cathodes, respectively, clearly showing the potential for utilizing Co$_3$O$_4$ catalysts in AEMFCs cathodes as an alternative to PGM catalysts. The difference in performance is also reflected in the resulting peak power densities (Figure 8b). While the Pt/C-Pt/C cell achieves 593 mW cm^{-2}, the Pt/C-Co$_3$O$_4$ + C cell reaches 388 mW cm^{-2}. This is a AEMFC performance that can be regarded as excellent, especially when compared to other reported performance values using Co-based cathode catalysts [15].

For the Pt-free cells using Co$_3$O$_4$ + C cathodes, the difference in performance between FSP Pd/CeO$_2$ + C and 10 wt % Pd/C-CeO$_2$ catalysts is very small (see Figure 8a). At 50 mA cm^{-2}, both Pd-based anodes show a cell voltage of 0.81 V, only 20 mV lower compared to the Pt/C anode. This is more clearly seen in Figure S7, which shows essentially identical mass activities above 0.8 V for these two Pt-free cells. This correlates well with the HOR activities measured in RDE (see Figure S6). At higher current densities the Pd-based AEMFCs also show excellent performance. At 0.5 A cm^{-2} the Pt/C, FSP Pd/CeO$_2$ + C and 10 wt % Pd/C-CeO$_2$ anodes resulted in cell voltages of 0.59 V, 0.53 V and 0.47 V, and peak power densities of 388, 309, 247 mW cm^{-2}, respectively. It is also noted that the new FSP Pd/CeO$_2$ catalyst synthesized from the one-pot FSP is highly active for HOR in AEMFCs. The performance is comparable or slightly higher than the 10 wt % Pd/C-CeO$_2$, which is considered to be the state-of-the-art Pt-free catalyst for AEMFCs [21]. Figure 8 and Figure S7 also show the performance of the PGM-free AEMFC based on the NiCo/C anode and Co$_3$O$_4$ + C cathode. The totally PGM-free cell achieves a peak power density of 22.1 mWcm^{-2}. Although this is a lower performance compared to the PGM based cells, the performance is in the same order of magnitude compared to other reported values in the literature for similar PGM free cells [23,24]. Comparing our AEMFC result using the NiCo-based anode with the RDE results, it is suggested that the performance of the NiCo AEMFC anode could be limited by mass transfer: While the RDE measurements show the NiCo catalysts having mass activities for the HOR in

the same order of magnitude as the PGM-based Pd/CeO$_2$ catalysts, e.g., 0.02 and 0.06 mA mg$^{-1}_{metal}$ at 0.05 V vs RHE, respectively, the mass activity is at least two orders of magnitude lower when the catalyst is used as an AEMFC anode (see Figures S6 and S7). In both cases the NiCo catalyst loading is approximately 10 times the loading of the PGM catalysts, e.g., RDE loadings of 500 μg Ni and 50 μg Pd, and AEMFC anode loadings of 5 mg cm^{-2} NiCo and 0.5 mg cm^{-2} Pd. The NiCo is therefore applied in much thicker catalyst layers with longer diffusion distances, which may in turn result in AEMFC anodes more sensitive to electrode flooding in the presence of liquid water [56].
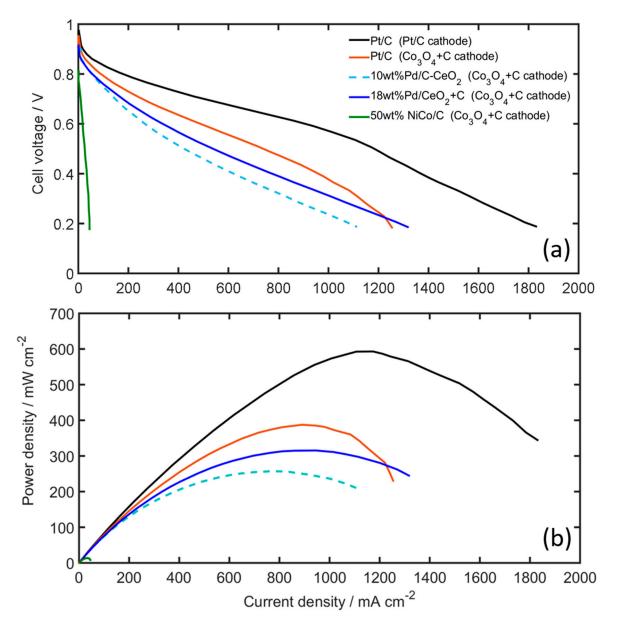

Figure 8. (**a**) Polarization, and (**b**) power density curves of the AEMFC using various anode and cathode catalysts (cathodes are denoted within parenthesis in the legend). Measurements taken at 70 °C, H$_2$ and O$_2$ on anode and cathode, using 1.0 and 0.5 slpm, respectively. Gas dew points are 68 and 73 °C for the anode and cathode, respectively.

3. Experimental

3.1. Catalyst Synthesis

3.1.1. Synthesis of Co_3O_4

Synthesis of fine powders of Co_3O_4 with nanoscale crystallinity was achieved via a modified version of the multi-stage method reported by Zhao-Qing et al. [57]. In the first stage, 90 mL of a 0.1 M (cobalt basis) solution of Cobalt Nitrate hexahydrate ($Co(NO_3)_2\cdot 6H_2O$) and Urea (NH_2CONH_2) at a molar ratio 1:5 of Co:Urea was placed in a PTFE-lined, 200 mL volume hydrothermal cell. This was reacted at 120 °C for 12 h and cooled to room temperature under ambient room conditions. This yielded a product phase of $Co_2(CO_3)OH_2$, which was washed with water to remove reaction residues. This powder was then ball-milled using spherical 5 mm zirconia milling media on a roller type mill to break down particle agglomerates. The milled powder was separated from the milling media, dried and decomposed via heat treatment at 250 °C in air to yield a final product phase of Co_3O_4. The final catalyst was produced at the ink preparation stage via mixing of Co_3O_4 with Vulcan XC-72 in a 50:50 ratio.

3.1.2. Synthesis of 10 wt % $Pd/C-CeO_2$ by Wet Chemistry

The synthesis and characterization of this state-of-the-art $Pd/C-CeO_2$ has been reported in detail elsewhere [18]. In summary, a composite consisting of C and CeO_2 was made by the addition of Vulcan XC-72 to a solution of $Ce(NO_3)_3\cdot 6H_2O$ in H_2O. The mixture was kept under stirring and sonication, the pH was adjusted to 12 with KOH, and the resulting suspension was stirred for 2 h. The product was separated by filtration and washed with H_2O until a neutral pH was obtained. The product was then dried at 65 °C, and subsequently heated under air in a tube furnace at 250 °C for 2 h. Cooling to room temperature was undertaken under a flow of Ar. The $C-CeO_2$ (4 g) composite was then suspended in water (500 mL), stirred vigorously for 30 min and sonicated for 20 min. To this mixture, a solution of K_2PdCl_4 (1.38 g) in water (60 mL) was slowly added (during ~1 h) under vigorous stirring, followed by addition of an aqueous solution of 2.5 M KOH (8.4 mL). Next, ethanol (50 mL) was added and the resulting mixture was heated at 80 °C for 60 min. The desired product of 10 wt % $Pd/C-CeO_2$ was filtered off, washed several times with distilled water to neutrality, and finally dried under vacuum at 65 °C until constant weight was reached.

3.1.3. Synthesis of FSP Pd/CeO_2 + C by Flame Spray Pyrolysis (FSP)

Nanoscale composite powders of Pd/CeO_2 were synthesized via single stage flame spray pyrolysis (FSP) of flammable precursor reagents: Appropriate stoichiometric quantities of Palladium Trimethyl Acetate and Cerium (II) 2-ethylhexanoate (49%) in 2-ethylhexanoic acid to produce an 18 wt % Pd/CeO_2 mixture were dissolved in xylene at a concentration of 0.13 M (total metals basis). Using a Tethis Nanotech NPS10 FSP unit, this solution was then atomized into a flame under a constant flow of air, which resulted in rapid high temperature combustion and atomization of the metal species. The product phases formed on cooling were collected from the airstream using a PTFE filter with ~0.5 μm pore size. For electrochemical testing the as-synthesized catalyst was mixed with Vulcan XC-72 during ink production. For RDE measurements a 50:50 ratio with XC72 was used, giving a 9.1:50:41.9 ratio of Pd:C:CeO_2. For full cell testing a ratio of 55:45 was used, giving a comparable 10:45:45 $Pd/C/CeO_2$ ratio to that of the state-of-the-art (SoA) $Pd/C-CeO_2$ catalyst produced via wet chemistry.

3.1.4. Synthesis of NiCo/C

The synthesis procedure for carbon-supported NiCo nanoparticles was adapted from that reported procedure [58] for the synthesis of monodispersed nickel nanoparticles. Stoichiometric quantities of Nickel (II) acetylacetonate (2.54 mmol), Cobalt (II) acetylacetonate (0.847 mmol) and VXC-72 carbon (200 mg) were mixed in a round-bottomed flask with oleylamine (63.8 mmol) and trioctylphosphine

(20.17 mmol), to give a final composition $Ni_{0.75}Co_{0.25}$ supported on carbon. Under an Ar atmosphere, the mixture was degassed for 30 min at 100 °C, then heated at a rate of 5 °C min^{-1} to 210 °C and held for 45 min. After cooling to room temperature, the resulting dispersion was washed multiple times with toluene and isopropyl alcohol with centrifugation, with a final wash of toluene and acetone. The resulting fine black powder was dried under vacuum and annealed for 2 h at 500 °C under an atmosphere of 5%H_2 in Ar.

3.2. Physical Characterization

3.2.1. XRD

X-ray diffraction was used to evaluate the crystallinity and phase composition of the catalysts and intermediates. Data were collected in transmission capillary mode using a Bruker D8 Advance A25 diffractometer, utilizing a Mo-Kα source, focusing Göbel mirror, and LynxEye XE™ detector. The phases were identified via matching with the ICDD PDF4+ (2017) database, and Whole Powder Pattern Modelling (WPPM) performed with the Bruker DiffracTopas v5 software suite. Crystallite sizes were calculated via the Integral Breadth method within the WPPM. For the carbon-supported NiCo nanoparticle sample, in order to correctly model the contribution of the carbon support, a separate scan was taken of the support, and a structureless model determined. This was included (with scaling) in the fitting of the supported NiCo.

3.2.2. TEM

Catalyst powders were prepared for transmission electron microscopy (TEM) by ultrasonication in isopropanol and dispersion on Cu grids with lacey carbon support film. Imaging was performed using three electron microscopes, a 30 kV, Hitachi S-5500 SEM/STEM, a 200 kV JEOL JEM-2100F and a 200 kV probe/image-corrected JEOL ARM-200F. Spectrum imaging using energy-dispersive X-ray spectroscopy (EDX) was performed on both the ARM-200F and JEM-2100F, and Electron Energy Loss Spectroscopy (EELS) was performed on the ARM-200F.

3.2.3. XPS

The X-ray Photoelectron Spectroscopy (XPS) measurements were recorded on a Kratos Analytical Axis Ultra DLD instrument with a monochromatized Al K$_\alpha$ X-ray source. A pass energy of 160 eV was used for survey scans in the range of 0–1200 eV. Detailed scans were conducted at a pass energy of 20 eV using a step size of 0.1 eV. The measured spectra were analyzed using casa XPS software (version 2.3.19), and a Lorentzian asymmetric (LA) line shape was used for each component. For measurement, the Pd-CeO_2 samples were dispersed on a borosilicate glass slide using high purity iso-propanol and were charge-neutralized during measurement using low energy electrons. For the Pd-CeO_2 sample binding energies were calibrated to the strong O1s (532.9 eV) line from the silicate substrate, whilst for NiCo adventitious carbon (284.8 eV) was used.

3.3. Rotating Disk Electrode (RDE) Characterization

Electrochemical catalyst characterization was performed using PINE Research RDE equipment. Measurements were performed in a PTFE cell using 0.1 M KOH solutions. A standard single junction Hg/HgO was used as the reference electrode, and a Pt foil was used as the counter electrode. All potentials were corrected to a standard reversible hydrogen electrode (RHE) by experimentally calibrating the Hg/HgO in hydrogen saturated 0.1 M KOH using a Pt electrode. A glassy carbon electrode (5 mm dia., 0.196 cm^2 geometrical surface area) embedded in a Teflon tip was used as the working electrode. The electrocatalytic activity of all catalysts was measured using a thin film approach where a catalyst suspension in H_2O, isopropyl alcohol and Nafion was drop-cast on the glassy carbon electrode and dried under a flow of Ar gas. For the determination of HOR and ORR activities, 99.999% purity H_2, and 99.9999% purity O_2 gases were used, respectively. Cycle voltammetry (CV) experiments

were recorded using 99.9999% purity Ar. The catalyst inks were prepared by taking an aliquot of 5 mg of the catalyst powder and suspended in a mixture of H_2O, isopropyl alcohol (H_2O: IPA, 1:1) and 30 μL of a 5.0% *w/w* lower aliphatic alcohol-water solution of Nafion (EW: 1100, Aldrich). After sonication for 30 min, the suspension (500 μg_{Ni} cm^{-2}) was dropped onto the GC electrode and dried at vacuum/nitrogen (N_2). Both 10 wt % Pd/C-CeO_2, and FSP Pd/CeO_2 + C catalyst inks were made in a similar way to NiCo/C, by keeping the loading as 50 μg_{Pd}.cm^{-2}. The VXC-72 carbon (50%) was physically mixed with the FSP Pd/CeO_2 while making the catalyst ink. For the ORR tests, the working electrode was preconditioned by cyclic sweeps from 0.05 V to 1.03 V vs RHE in an already Ar-purged electrolyte (purged for 30 min) at 100 mV/s for 40 sweeps, and at 10 mV/s for 5 sweeps. The background (capacitance) current was measured at 20 mV/s for 20 sweeps with an electrode rotation of 1600 rpm. EIS measurements between 10 kHz and 1 Hz at 0.5 V vs RHE with an amplitude of 0.01 V were conducted to correct for the iR contribution. Both the background and iR contributions were later subtracted from the raw data. The ORR measurements were carried out 5 times between 1.03 V and 0.05 V vs RHE at 20 mV/s with an electrode rotation of 1600 rpm, and the Pt-ring potential was set to 1.2 V vs RHE. Similarly, for the HOR tests, the working electrodes were preconditioned by cycling the potential between −0.2 and 0.4 V vs RHE for 50 cycles in an Ar-purged electrolyte and kept under an Ar atmosphere at a sweep rate of 20 mV s^{-1}. The Ar atmosphere and the upper potential limit was selected in order to minimize possible effects of surface passivation on the catalysts. After the preconditioning, CVs were collected by sweeping the potential between −0.06 and 0.4V at 1 mVs^{-1} under similar conditions (argon sparging and atmosphere). The electrolyte was subsequently saturated with H_2, and the HOR polarization curves were recorded in the potential range −0.06 through 0.4 V at a scan rate of 1mVs^{-1} with the electrode rotating at 1600 rpm. The solutions were continuously sparged with H_2 during these experiments. In addition, the HOR activity was further assessed by linear sweep voltammetry (LSV) in the hydrogen-saturated electrolyte. For these LSVs the scan rate was 5mVs^{-1} and the potential range was from −0.06 through 0.4 V. LSVs were recorded at a range of rotation speeds from 400 through 2400 rpm.

3.4. Membrane Electrode Assembly (MEA) Preparation and Evaluation

Gas diffusion layers (GDLs)—GDL340 carbon paper with micro porous layer (MPL) supplied by CeTech Co., Ltd., (Taiwan, China) were selected as GDLs for both anode and cathode sides, similar to those used in our previous study [16]. The GDL properties are summarized in Table 2. The anion exchange membrane (AEM) and ionomer used were AT-1 and aQAPS-S$_{14}$, respectively (supplied by Hephas Energy Co., (China). The AT-1 membrane with a thickness of 30–40 μm in the dry form has a specific ion conductivity of ca. 0.1 S cm^{-1} at 60 °C. The main structure of AT-1 membrane and aQAPS-S-$_{14}$ ionomer contains quaternary ammonium groups, enabling the bonding of polysulfone backbone via CH_2 bridges and the attachment of hydrophobic side chains onto the backbone to obtain the ion-aggregating structure [59].

Table 2. Physical properties of GDL340.

Thickness (mm)	PTFE (wt %)		Air Permeability (s)	Through Plane Resistance (mΩ cm^2)	Mean Pore Diameter (μm)	Porosity (%)	Contact Angle (°)	
	MPL	Back					MPL	Back
0.31	30	30	99.5	11.9	36.69	64.06	146.2	147.5

The catalyst ink was prepared by blending the corresponding catalyst powders with 20 wt % aQAPS-S$_{14}$ ionomer (2 wt % DMF). The catalyst and ionomer were mixed with deionized (DI) water and isopropyl alcohol (IPA) with a volume ratio of 1:1 as dispersant/solvent, according to previous ink compositions and preparation methods [60]. For the FSP Pd/CeO_2 and Co_3O_4 catalysts, 50 wt % carbon supports (Vulcan XC-72) was added during catalyst ink preparation to form Co_3O_4 + C and Pd/CeO_2 + C composites, respectively. As an example, a typical FSP Pd/CeO_2 + C catalyst ink preparation was made by mixing 29.6 mg carbon dispersed into 865 mg DI water and sonicated for 30 min. An amount

of 36.1 mg of 18 wt % Pd/CeO_2 was then added to the carbon dispersion and sonicated for an additional 30 min. Then, 657 mg of ionomer was added to the suspension, followed by adding 865 mg IPA. The mixture was sonicated for 60 min before spray coating it onto a 13 cm^2 GDL340 surface on a hot plate pre-heated at 80 °C. For comparative purposes, an MEA prepared with 40% Pt/C (Tanaka) on both anode and cathode was also prepared. The catalyst loadings of each AEMFC are presented in Table 3.

Table 3. Anode and cathode composition of tested membrane electrode assemblies (MEAs).

Tittle	Anodes				Cathodes			
Cell	Catalyst	Pt, Pd or NiCo Loading (mg cm^{-2})	Carbon/Ceria Loading (mg cm^{-2})	Ionomer Loading (mg cm^{-2})	Catalyst	Pt or Co$_3$O$_4$ Loading (mg cm^{-2})	Carbon Loading (mg cm^{-2})	Ionomer Loading (mg cm^{-2})
1	40% Pt/C	0.5	0.75	0.25	40% Pt/C	0.5	0.75	0.25
2	40% Pt/C	0.5	0.75	0.25	Co$_3$O$_4$ + C	3	3	1.2
3	10% Pd/C CeO$_2$	0.5	2.25/2.25	1	Co$_3$O$_4$ + C	3	3	1.2
4	18% Pd/CeO$_2$ + C	0.5	2.27/2.27	1	Co$_3$O$_4$ + C	3	3	1.2
5	50% NiCo/C	5.0	5	5	Co$_3$O$_4$ + C	3	3	1.2

In order to ion exchange the membranes into the hydroxide form, the as-received membranes were pre-treated by soaking in 1 M KOH for at least 48 h at 60 °C. The prepared gas diffusion electrodes (GDEs) were also dipped in 1 M KOH solution for 24 h before the assembly of the AEMFC. Finally, the AT-1 AEM was sandwiched with two prepared GDEs with 10.24 cm^{-2} active area. The obtained MEAs were sandwiched between two graphite plates with triple serpentine flow fields (1 mm channel width and height, 1.5 mm land width) and gold-coated copper current collector plates, 250–300 μm thick Teflon gaskets, and compressed using 1.47 N m of torque to each of the eight screws. A fuel cell testing system (FCED-PD50 test station, Asia Pacific Fuel Cell Technologies, Ltd.) was employed. The polarization curves were recorded while operating the cell under 1.0 and 0.5 slpm of H_2 and O_2, respectively.

4. Conclusions

This paper presents our research progress in developing Pt-free and PGM-free catalysts used in AEMFCs. Non-noble Co_3O_4 catalysts with nanoscale crystallinity and an anisotropic platelet morphology have been synthesized via a scalable process. Although less active compared to the PGM-based Pt/C catalyst according to the RRDE experiments, these Co_3O_4 catalysts show an excellent AEMFC performance, with only a 100 mV decrease at 0.5 A cm^{-2} measured relative to Pt/C.

The scalable FSP synthesis of an extremely active nano-scaled Pd/CeO_2 material is also reported. This material shows no apparent Pd crystallinity and extremely small (~1 nm) Pd nanoparticles. The XPS data of the FSP-synthesized Pd/CeO_2 shows no evidence of metallic Pd, and only a weak signal which may be attributed to a PdO-type Pd(II). Although not conclusively proven, the FSP Pd/CeO_2 may present Pd^{4+} bulk oxide and/or some interaction between the catalyst and CeO_2 support. Nevertheless, the FSP Pd/CeO_2 + C catalyst showed consistently excellent catalytic activity towards the HOR, performing just as well as, or better than, the state-of-the-art 10 wt % $Pd/C-CeO_2$ catalyst in both RDE and AEMFC measurements. AEMFC tests using FSP Pd/CeO_2 + C and Co_3O_4/C as the anode and cathode catalysts, respectively, achieved a peak power density as high as 308 mW cm^{-2}.

Monodispersed NiCo nanoparticles supported on carbon (NiCo/C) are shown to perform in the same order of magnitude as for the Pt and Pd based HOR catalysts in RDE below 0.3 V. However, beyond 0.3 V there is a sharp decline in the NiCo/C current, presumably owing to reactions forming NiOH and $Ni(OH)_2$ at the catalyst surface as previously reported. In the AEMFC, however, the NiCo/C catalysts showed two orders of magnitude lower performance with respect to the PGM-based catalysts. It is likely to be due to uneven reaction rates in the much thicker catalytic layer in the fuel cell causing severe mass transfer effects in the electrode. The use of such PGM-free catalysts in real AEMFCs

may require higher catalysts loadings, naturally resulting in thicker catalysts layers, and hence it is important that further development in PGM-free HOR catalysts not only considers catalytic activity, but also electrode composition, morphology, as well as operating AEMFC conditions when evaluating catalysts for this application.

References

1. Varcoe, J.R.; Atanassov, P.; Dekel, D.R.; Herring, A.M.; Hickner, M.A.; Kohl, P.A.; Kucernak, A.R.; Mustain, W.E.; Nijmeijer, K.; Scott, K.; et al. Anion-exchange membranes in electrochemical energy systems. *Energy Environ. Sci.* **2014**, *7*, 3135–3191. [CrossRef]

2. Gottesfeld, S.; Dekel, D.R.; Page, M.; Bae, C.; Yan, Y.; Zelenay, P.; Kim, Y.S. Anion exchange membrane fuel cells: Current status and remaining challenges. *J. Power Sources* **2018**, *375*, 170–184. [CrossRef]

3. Burchardt, T.; Gouérec, P.; Sanchez-Cortezon, E.; Karichev, Z.; Miners, J.H. Alkaline fuel cells: Contemporary advancement and limitations. *Fuel* **2002**, *81*, 2151–2155. [CrossRef]

4. Kostowskyj, M.A.; Gilliam, R.J.; Kirk, D.W.; Thorpe, S.J. Silver nanowire catalysts for alkaline fuel cells. *Int. J. Hydrogen Energy* **2008**, *33*, 5773–5778. [CrossRef]

5. Osgood, H.; Devaguptapu, S.V.; Xu, H.; Cho, J.; Wu, G. Transition metal (Fe, Co, Ni, and Mn) oxides for oxygen reduction and evolution bifunctional catalysts in alkaline media. *Nano Today* **2016**, *11*, 601–625. [CrossRef]

6. Xin, L.; Wang, Z.; Qi, J.; Li, W. Carbon supported Ag nanoparticles as high performance cathode catalyst for H_2/O_2 anion exchange membrane fuel cell. *Front. Chem.* **2013**, *16*, 1–5. [CrossRef] [PubMed]

7. Dekel, D.R. Alkaline Membrane Fuel Cell (AMFC) Materials and System Improvement—State-of-the-Art. *ECS Trans.* **2013**, *50*, 2051–2052. [CrossRef]

8. Erikson, H.; Sarapuu, A.; Tammeveski, K. Oxygen Reduction Reaction on Silver Catalysts in Alkaline Media: A Minireview. *ChemElectroChem* **2019**, *6*, 73–86. [CrossRef]

9. Zhao, S.; Yan, L.; Luo, H.; Mustain, W.; Xu, H. Recent progress and perspectives of bifunctional oxygen reduction/evolution catatalyst development for regenerative anion exchange membrane fuel cells. *Nano Energy* **2018**, *47*, 172–198. [CrossRef]

10. Durst, J.; Siebel, A.; Simon, C.; Hasche, F.; Herranz, J.; Gasteiger, H. New insights into the electrochemical hydrogen oxidation and evolution reaction mechanism. *Energy Environ. Sci.* **2014**, *7*, 2255–2260. [CrossRef]

11. Dekel, D.R. Unraveling mysteries of hydrogen electrooxidation in anion exchange membrane fuel cells. *Curr. Opin. Electrochem.* **2018**, *12*, 182–188. [CrossRef]

12. Xu, J.; Gao, P.; Zhao, T. Non-precious Co_3O_4 nano-rod electrocatalyst for oxygen reduction reaction in anion-exchange membrane fuel cells. *Energy Environ. Sci.* **2012**, *5*, 5333–5339. [CrossRef]

13. Wang, D.-C.; Huang, N.-B.; Sun, Y.; Zhan, S.; Zhang, J.-J. GO clad Co_3O_4 (Co_3O_4@GO) as ORR catalyst of anion exchange membrane fuel cell. *Int. J. Hydrogen Energy* **2017**, *42*, 20216–20223. [CrossRef]

14. Liang, Y.; Li, Y.; Wang, H.; Zhou, J.; Wang, J.; Regier, T.; Dai, H. Co_3O_4 nanocrystals on graphene as a synergistic catalyst for oxygen reduction reaction. *Nat. Mater.* **2011**, *10*, 780. [CrossRef] [PubMed]

15. Mamlouk, M.; Kumar, S.S.; Gouerec, P.; Scott, K. Electrochemical and fuel cell evaluation of Co based catalyst for oxygen reduction in anion exchange polymer membrane fuel cells. *J. Power Sources* **2011**, *196*, 7594–7600. [CrossRef]

16. Truong, V.M.; Wang, C.-L.; Yang, M.; Yang, H. Effect of tunable hydrophobic level in the gas diffusion substrate and microporous layer on anion exchange membrane fuel cells. *J. Power Sources* **2018**, *402*, 301–310. [CrossRef]

17. Davydova, E.S.; Mukerjee, S.; Jaouen, F.; Dekel, D.R. Electrocatalysts for hydrogen oxidation reaction in alkaline electrolytes. *ACS Catal.* **2018**, *8*, 6665–6690. [CrossRef]

18. Miller, H.A.; Lavacchi, A.; Vizza, F.; Marelli, M.; Di Benedetto, F.; D'Acapito, F.; Paska, Y.; Page, M.; Dekel, D.R. A Pd/C-CeO_2 Anode Catalyst for High-Performance Platinum-Free Anion Exchange Membrane Fuel Cells. *Angew. Chem. Int. Ed.* **2016**, *55*, 6004–6007. [CrossRef]

19. Alesker, M.; Page, M.; Shviro, M.; Paska, Y.; Gershinsky, G.; Dekel, D.R.; Zitoun, D. Palladium/nickel bifunctional electrocatalyst for hydrogen oxidation reaction in alkaline membrane fuel cell. *J. Power Sources* **2016**, *304*, 332–339. [CrossRef]

20. Dekel, D.R. Review of cell performance in anion exchange membrane fuel cells. *J. Power Sources* **2018**, *375*, 158–169. [CrossRef]

21. Omasta, T.J.; Peng, X.; Miller, H.A.; Vizza, F.; Wang, L.; Varcoe, J.R.; Dekel, D.R.; Mustain, W.E. Beyond 1.0 W cm^{-2} performance without platinum: The beginning of a new era in anion exchange membrane fuel cells. *J. Electrochem. Soc.* **2018**, *165*, J3039–J3044. [CrossRef]

22. Davydova, E.; Zaffran, J.; Dhaka, K.; Toroker, M.; Dekel, D. Hydrogen Oxidation on Ni-Based Electrocatalysts: The Effect of Metal Doping. *Catalysts* **2018**, *8*, 454. [CrossRef]

23. Lu, S.; Pan, J.; Huang, A.; Zhuang, L.; Lu, J. Alkaline polymer electrolyte fuel cells completely free from noble metal catalysts. *Proc. Natl. Acad. Sci. USA* **2008**, *105*, 20611–20614. [CrossRef]

24. Hu, Q.; Li, G.; Pan, J.; Tan, L.; Lu, J.; Zhuang, L. Alkaline polymer electrolyte fuel cell with Ni-based anode and Co-based cathode. *Int. J. Hydrogen Energy* **2013**, *38*, 16264–16268. [CrossRef]

25. Kabir, S.; Lemire, K.; Artyushkova, K.; Roy, A.; Odgaard, M.; Schlueter, D.; Oshchepkov, A.; Bonnefont, A.; Savinova, E.; Sabarirajan, D.C. Platinum group metal-free NiMo hydrogen oxidation catalysts: High performance and durability in alkaline exchange membrane fuel cells. *J. Mater. Chem. A* **2017**, *5*, 24433–24443. [CrossRef]

26. Roy, A.; Talarposhti, M.R.; Normile, S.J.; Zenyuk, I.V.; De Andrade, V.; Artyushkova, K.; Serov, A.; Atanassov, P. Nickel–copper supported on a carbon black hydrogen oxidation catalyst integrated into an anion-exchange membrane fuel cell. *Sustain. Energy Fuels* **2018**, *2*, 2268–2275. [CrossRef]

27. Knop, O.; Reid, K.; Sutarno; Nakagawa, Y. Chalcogenides of the transition elements. VI. X-Ray, neutron, and magnetic investigation of the spinels Co_3O_4, $NiCo_2O_4$, Co_3S_4, and $NiCo_2S_4$. *Can. J. Chem.* **1968**, *46*, 3463–3476. [CrossRef]

28. Ivanov, V.K.; Shcherbakov, A.B.; Usatenko, A. Structure-sensitive properties and biomedical applications of nanodispersed cerium dioxide. *Russ. Chem. Rev.* **2009**, *78*, 855. [CrossRef]

29. Paparazzo, E. On the curve-fitting of XPS Ce(3d) spectra of cerium oxides. *Mater. Res. Bull.* **2011**, *46*, 323–326. [CrossRef]

30. Burroughs, P.; Hamnett, A.; Orchard, A.F.; Thornton, G. Satellite structure in the X-ray photoelectron spectra of some binary and mixed oxides of lanthanum and cerium. *J. Chem. Soc. Dalton Trans.* **1976**, *17*, 1686–1698. [CrossRef]

31. Sharma, S.; Mukri, B.D.; Hegde, M. Direct evidence of redox interaction between metal ion and support oxide in $Ce_{0.98}Pd_{0.02}O_{2-\delta}$ by a combined electrochemical and XPS study. *Dalton Trans.* **2011**, *40*, 11480–11489. [CrossRef] [PubMed]

32. Brun, M.; Berthet, A.; Bertolini, J. XPS, AES and Auger parameter of Pd and PdO. *J. Electron Spectrosc. Relat. Phenom.* **1999**, *104*, 55–60. [CrossRef]

33. Shafeev, G.; Themlin, J.M.; Bellard, L.; Marine, W.; Cros, A. Enhanced adherence of area-selective electroless metal plating on insulators. *J. Vac. Sci. Technol. A Vac. Surf. Film.* **1996**, *14*, 319–326. [CrossRef]

34. Kim, K.S.; Gossmann, A.; Winograd, N. X-ray photoelectron spectroscopic studies of palladium oxides and the palladium-oxygen electrode. *Anal. Chem.* **1974**, *46*, 197–200. [CrossRef]

35. Li, L.; Zhang, N.; He, H.; Zhang, G.; Song, L.; Qiu, W. Shape-controlled synthesis of Pd nanocrystals with exposed {110} facets and their catalytic applications. *Catal. Today* **2019**, *327*, 28–36. [CrossRef]

36. Priolkar, K.; Bera, P.; Sarode, P.; Hegde, M.; Emura, S.; Kumashiro, R.; Lalla, N. Formation of $Ce_{1-x}Pd_xO_{2-\delta}$ Solid Solution in Combustion-Synthesized Pd/CeO_2 Catalyst: XRD, XPS, and EXAFS Investigation. *Chem. Mater.* **2002**, *14*, 2120–2128. [CrossRef]

37. Mason, M.; Gerenser, L.; Lee, S.-T. Electronic structure of catalytic metal clusters studied by X-ray photoemission spectroscopy. *Phys. Rev. Lett.* **1977**, *39*, 288. [CrossRef]

38. Zhou, W.P.; Lewera, A.; Larsen, R.; Masel, R.I.; Bagus, P.S.; Wieckowski, A. Size effects in electronic and catalytic properties of unsupported palladium nanoparticles in electrooxidation of formic acid. *J. Phys. Chem. B* **2006**, *110*, 13393–13398. [CrossRef]

39. Nishizawa, T.; Ishida, K. The Co−Ni (Cobalt-Nickel) system. *Bull. Alloy Phase Diagr.* **1983**, *4*, 390–395. [CrossRef]

40. Houska, C.R.; Averbach, B.L.; Cohen, M. The cobalt transformation. *Acta Metall.* **1960**, *8*, 81–87. [CrossRef]

41. Kitakami, O.; Sato, H.; Shimada, Y.; Sato, F.; Tanaka, M. Size Effect on the Crystal Phase of Cobalt Fine. *Phys. Rev. B* **1997**, *56*, 13849. [CrossRef]

42. Moreau, L.M.; Ha, D.-H.; Bealing, C.R.; Zhang, H.; Hennig, R.G.; Robinson, R.D. Unintended phosphorus doping of nickel nanoparticles during synthesis with TOP: A discovery through structural analysis. *Nano Lett.* **2012**, *12*, 4530–4539. [CrossRef] [PubMed]

43. Grosvenor, A.P.; Biesinger, M.C.; Smart, R.S.C.; McIntyre, N.S. New interpretations of XPS spectra of nickel metal and oxides. *Surf. Sci.* **2006**, *600*, 1771–1779. [CrossRef]

44. Roberts, M.W.; Smart, R.S.C. The defect structure of nickel oxide surfaces as revealed by photoelectron spectroscopy. *J. Chem. Soc. Faraday Trans. 1 Phys. Chem. Condens. Phases* **1984**, *80*, 2957–2968. [CrossRef]

45. Carley, A.; Jackson, S.; O'shea, J.; Roberts, M. The formation and characterisation of Ni3+—an X-ray photoelectron spectroscopic investigation of potassium-doped Ni (110)–O. *Surf. Sci.* **1999**, *440*, L868–L874. [CrossRef]

46. Li-Shing, H.; Williams, R.S. Electronic-structure study of the Ni Ga and the Ni In intermetallic compounds using X-ray photoemission spectroscopy. *J. Phys. Chem. Solids* **1994**, *55*, 305–312. [CrossRef]

47. McIntyre, N.; Cook, M. X-ray photoelectron studies on some oxides and hydroxides of cobalt, nickel, and copper. *Anal. Chem.* **1975**, *47*, 2208–2213. [CrossRef]

48. Schenck, C.; Dillard, J.; Murray, J. Surface analysis and the adsorption of Co (II) on goethite. *J. Colloid Interface Sci.* **1983**, *95*, 398–409. [CrossRef]

49. Chuang, T.; Brundle, C.; Rice, D. Interpretation of the x-ray photoemission spectra of cobalt oxides and cobalt oxide surfaces. *Surf. Sci.* **1976**, *59*, 413–429. [CrossRef]

50. Chen, R.; Yang, C.; Cai, W.; Wang, H.-Y.; Miao, J.; Zhang, L.; Chen, S.; Liu, B. Use of Platinum as the Counter Electrode to Study the Activity of Nonprecious Metal Catalysts for the Hydrogen Evolution Reaction. *ACS Energy Lett.* **2017**, *2*, 1070–1075. [CrossRef]

51. Chen, J.G.; Jones, C.W.; Linic, S.; Stamenkovic, V.R. Best Practices in Pursuit of Topics in Heterogeneous Electrocatalysis. *ACS Catal.* **2017**, *7*, 6392–6393. [CrossRef]

52. Campos-Roldán, C.; González-Huerta, R.; Alonso-Vante, N. Experimental protocol for HOR and ORR in alkaline electrochemical measurements. *J. Electrochem. Soc.* **2018**, *165*, J3001–J3007. [CrossRef]

53. Davydova, E.S.; Speck, F.D.; Paul, M.T.Y.; Dekel, D.R.; Cherevko, S. Stability Limits of Ni-Based Hydrogen Oxidation Electrocatalysts for Anion Exchange Membrane Fuel Cells. *ACS Catal.* **2019**, *9*, 6837–6845. [CrossRef]

54. Alsabet, M.; Grden, M.; Jerkiewicz, G. Electrochemical growth of surface oxides on nickel. Part 1: Formation of α-$Ni(OH)_2$ in relation to the polarization potential, polarization time, and temperature. *Electrocatalysis* **2011**, *2*, 317–330. [CrossRef]

55. Alsabet, M.; Grdeń, M.; Jerkiewicz, G. Electrochemical growth of surface oxides on nickel. Part 3: Formation of β-NiOOH in relation to the polarization potential, polarization time, and temperature. *Electrocatalysis* **2015**, *6*, 60–71. [CrossRef]

56. Darab, M.; Barnett, A.O.; Lindbergh, G.; Thomassen, M.S.; Sunde, S. The influence of catalyst layer thickness on the performance and degradation of PEM fuel cell cathodes with constant catalyst loading. *Electrochim. Acta* **2017**, *232*, 505–516. [CrossRef]

57. Liu, Z.-Q.; Xu, Q.-Z.; Wang, J.-Y.; Li, N.; Guo, S.-H.; Su, Y.-Z.; Wang, H.-J.; Zhang, J.-H.; Chen, S. Facile hydrothermal synthesis of urchin-like $NiCo_2O_4$ spheres as efficient electrocatalysts for oxygen reduction reaction. *Int. J. Hydrogen. Energy* **2013**, *38*, 6657–6662. [CrossRef]

58. Carenco, S.; Boissiere, C.; Nicole, L.; Sanchez, C.; Le Floch, P.; Mézailles, N. Controlled design of size-tunable monodisperse nickel nanoparticles. *Chem. Mater.* **2010**, *22*, 1340–1349. [CrossRef]

59. Pan, J.; Chen, C.; Li, Y.; Wang, L.; Tan, L.; Li, G.; Tang, X.; Xiao, L.; Lu, J.; Zhuang, L. Constructing ionic highway in alkaline polymer electrolytes. *Energy Environ. Sci.* **2014**, *7*, 354–360. [CrossRef]

60. Lindström, R.W.; Kortsdottir, K.; Wesselmark, M.; Oyarce, A.; Lagergren, C.; Lindbergh, G. Active Area Determination of Porous Pt Electrodes Used in Polymer Electrolyte Fuel Cells: Temperature and Humidity Effects. *J. Electrochem. Soc.* **2010**, *157*, B1795–B1801. [CrossRef]